Toughening of soda-lime-silica glass by nanoscale phase separation: Molecular dynamics study

Johan F. S. Christensen,[1] Søren S. Sørensen,[1] Theany To,[1] Mathieu Bauchy,[2] and Morten M. Smedskjaer[1,*]

[1]*Department of Chemistry and Bioscience, Aalborg University, 9220 Aalborg, Denmark*

[2]*Department of Civil and Environmental Engineering, University of California, Los Angeles, California 90095, USA*

(Received 23 February 2021; revised 19 June 2021; accepted 18 August 2021; published 7 September 2021)

The low fracture toughness of oxide glasses is a key limitation for many of their applications. Inducing and controlling nanoscale phase separation in oxide glasses has been proposed as a potential toughening strategy, as, unlike many alternative extrinsic toughening approaches, it allows one to retain the optical transparency. Using molecular dynamics simulations, we here investigate the toughening mechanism in soda-lime-silica glasses with embedded glassy nanoscale silica droplets. This system is chosen as a model for the experimental structure of phase-separated soda-lime-silica glass, which is attractive considering its existing commercial use and the ease of inducing phase separation. We calculate the fracture toughness of glass structures containing nanodroplets of varying sizes and with different precrack positions, revealing that the glassy silica droplets toughen the material. The simulations show that crack propagation is impeded by crack arrest, crack deflection and diversion, and stress field alteration, ultimately increasing the fracture toughness. Our findings thus shed light on the toughening mechanism due to phase separation, with important implications for the experimental design of oxide glasses with controlled nanoscale phase separation.

DOI: 10.1103/PhysRevMaterials.5.093602

I. INTRODUCTION

Resistance to crack initiation and propagation is an important feature for many applications of oxide glasses, motivating the development of materials with enhanced strength and toughness [1]. Strong and tough glasses would allow manufacturers to produce thinner glass products, ultimately reducing the cost and environmental footprint of glass manufacturing. Furthermore, it would improve safety by reducing the number of injuries related to glass fracture and would also open up for new innovative glass products. Although oxide glasses are intrinsically strong, their practical strength is greatly reduced due to the presence of surface flaws and cracks that inevitably form during manufacturing or usage, thus reducing the material's resistance to breakage. During a tensile loading event, the applied stress is concentrated at the flaw or crack tips. This makes oxide glasses vulnerable to crack growth, especially given their low fracture toughness, which in turn is related to their inherent brittleness. While ductile materials are primarily intrinsically toughened, i.e., ductility (e.g., through dislocations) enables limited plastic deformation dissipating the local stress that would otherwise cause crack growth [2], brittle materials such as oxide glasses lack such mechanism. This makes brittle materials prone to crack growth and thus reduces their strength.

The fracture toughness and degree of brittleness of oxide glasses vary with the chemical composition, thus making it possible to develop tougher oxide glasses by compositional design. However, the number of possible glass compositions is colossal [3] and the variation in fracture toughness of oxide glasses is relatively small (typically 0.5 to 1.0 MPa $m^{1/2}$ [4]). Besides composition optimization, multiple alternative strategies to toughen oxide glasses have thus been investigated. The introduction of compressive surface stress, e.g., by thermal tempering or chemical tempering by ion exchange, can greatly improve the resistance of the material to breakage as the formed surface stress counteracts the opening of surface cracks [1,5]. The presence of another phase in the glass can also induce toughening by arresting or diverting cracks at the phase interfaces and hereby impede the crack propagation [6]. This is exploited in glass ceramics which are toughened due to the presence of crystallites embedded in the glass matrix [7,8]. Glass ceramics are typically produced by a controlled two-step heat treatment to induce nucleation and crystal growth [9]. Crystallization often leads to a loss of transparency, but it can be avoided if the size of the crystallites is much smaller than the wavelength of visible light or the refractive indexes of glass and crystal are similar and the crystal possesses low birefringence [10]. Crystallites can also be introduced to glassy materials by alternative methods such as implanting nanoparticles into an oxide glass matrix [11], thus forming a composite material.

Phase separation is another potential method for extrinsic toughening of oxide glasses, as phase-separated glasses comprise two or more glassy phases, leading to potential toughening of the material similar to the mechanism observed in glass ceramics. However, the mechanical properties of phase-separated glasses have not been studied to the same extent as those of glass ceramics, with only a few reported studies [12–14]. For example, Seal *et al.* [14] found that the indentation toughness increased for a sodium borosilicate glass when forming an interconnected network of glassy phases, whereas it decreased when glassy droplets were formed. Yet, we note that the fracture toughness determination by Vickers indentation is generally problematic [15]. Moreover, the

*mos@bio.aau.dk

fracture patterns of phase-separated glasses have also recently been studied by peridynamic simulations, revealing that toughening can be induced by both soft spherical particles in a stiff matrix and vice versa [16]. Therefore, further investigations are needed to understand the effect of phase separation on glass mechanical properties and elucidate the underlying toughening mechanisms.

Liquid-liquid phase separation is a well-known phenomenon in many oxide glass systems [17–21]. It occurs due to liquid-liquid immiscibility, allowing for phase separation at temperatures above the glass transition temperature while still below the immiscibility temperature, ultimately yielding phase-separated glasses consisting of two or more disordered phases upon quenching. Depending on the temperature and chemical composition of the system (i.e., also Gibbs free energy), phase separation can occur by "nucleation and growth" or "spinodal decomposition," yielding discrete droplets or an interconnected network, respectively [21,22]. Such glass-in-glass systems may have two or more glass transition temperatures and the phenomenon can be used to tailor the microstructure, as done in, e.g., Vycor® glass [23]. The structures formed by phase separation can cause light scattering and thus result in loss of transparency [24]. However, the transparency can be retained when the size of the formed structures is small relative to the wavelength of visible light [18], equivalent to the case of some glass ceramics. For various glass-forming oxide systems, it has been shown that the size of droplets formed by phase separation can be controlled by adjusting the composition and thermal history, enabling the synthesis of finely controlled phase-separated oxide glasses [17,18]. This makes phase separation a promising approach for preparing tough, transparent oxide glasses.

Soda-lime-silica (SLS) glass is a good model system for understanding the effect of phase separation on fracture toughness, considering its well-understood structure, numerous commercial applications, and the fact that nanoscale droplets can be formed in SLS glasses [17]. Furthermore, phase separation is prone to occur in a large compositional space of SLS glass systems [17,22,25]. However, to our knowledge, the effect of phase separation on the fracture toughness in SLS glasses has not yet been investigated, neither by experiments nor simulations. In this study, we use classical molecular dynamics (MD) simulations to predict and understand the fracture behavior of SLS glasses containing nanodroplets that can be formed by phase separation. The computational cost of atomistic simulations limits the simulation time, precluding simulation of the actual nanoscale phase separation process in the SLS glasses; thus, we employ an alternative procedure where we combine two homogeneous glass structures to form phase-separated systems. We study the effect of spherical particles with diameters of 2 to 4 nm on the mechanical properties; consequently, we are restricted to systems containing a small number of droplets due to the computational cost. Specifically, we study systems that resemble the phase-separated glasses studied in detail by Burnett and Douglas [17]. They showed that phase separation can be controlled at the nanoscale for various glasses in the Na_2O–CaO–SiO_2 system, with the phase separation yielding droplets or alternatively connected structures of almost pure silica in a modifier-rich matrix. We thus simulate systems comprised of glassy droplets of pure silica (SiO_2) in an SLS glass matrix. To this end, we simulate both a series of phase-separated glasses with a constant matrix composition of $12.5Na_2O$–$12.5CaO$–$75SiO_2$ as well as a phase-separated glass having an average composition of $12.5Na_2O$–$12.5CaO$–$75SiO_2$, where the latter corresponds to one of the systems studied by Burnett and Douglas [17]. The phase-separated glasses of constant matrix composition have average compositions of $(50-x/2)Na_2O$–$(50-x/2)CaO$–$xSiO_2$ for $x = 75.3$, 76.2, and 77.7. These glasses are thus all in the compositional range for which Burnett and Douglas [17] observed droplets formed by phase separation. Our study reveals the atomic scale toughening mechanisms by exploiting the advantages of MD simulations, as we study well-controlled and idealized systems and observe nanoscale crack propagation, crack-particle interactions, and local stress buildup. The insight into the toughening mechanisms can guide future experimental work and pave the way for the development of tough, yet transparent oxide glasses.

II. COMPUTATIONAL METHODS

A. Simulation details

All MD simulations have been performed using an interatomic potential of the Buckingham type combined with long-range Coulombic interactions. The parameters for the interatomic potential were adopted from Xiang and Du [26], who used the parameters originally developed by Teter [27] and later modified and extended to include calcium [28]. This potential has previously been found to provide good replication of the structure of SLS and sodium silicate glasses [29–31]. A cutoff distance of 8 Å was used for the short-range Buckingham interactions, while the long-range Coulombic interactions were solved using the particle-particle particle-mesh algorithm with a relative precision of 10^{-5} and a cutoff between the calculations in real and inverse space of 25 Å. For all simulations, a fixed time step of 1 fs and periodic boundary conditions were used. Nosé-Hoover thermo- and barostats were used when applicable. All simulations in the NPT ensemble were performed at zero pressure unless otherwise stated. All energy minimizations were performed using the conjugate gradient method. The simulations were performed using the LAMMPS software [32] utilizing graphics processing unit (GPU) acceleration [33,34]. Illustrations of the molecular structure were made using the OVITO software [35]. All simulations have been independently reproduced six times for statistical averaging of results, except for the glasses quenched at lower cooling rates as described in Sec. II B.

B. Preparation of homogeneous and phase-separated glasses

The following procedure was used to prepare homogeneous silica, SLS-71.9, SLS-73.3, and SLS-75.0 glasses (see the molar compositions in Table I). Approximately 20 000 atoms were randomly placed in a cubic simulation box while ensuring a minimum distance of 2 Å between the atoms. The size of the simulation box was set so that the initial density was equal to 1.7 and 2.1 g/cm^3 for SLS and silica glasses, respectively. An energy minimization was performed,

TABLE I. Glass ID, average chemical composition, and details of the phase-separated systems for the seven studied glass compositions. All compositions have been studied as homogeneous glasses, while phase-separated systems of only the SLS-75.0, SLS-75.3, SLS-76.2, and SLS-77.7 compositions have been simulated. The matrix and droplet phases are indicated for the phase-separated glasses, and D_{droplet} and vol $\%_{\text{droplet}}$ are the droplet diameter and volume percentage of the droplet phase, respectively.

	Average composition			Details for phase-separated system			
Glass ID	Na_2O (mol%)	CaO (mol%)	SiO_2 (mol%)	Matrix phase	Droplet phase	D_{droplet} (nm)	vol$\%_{\text{droplet}}$ (%)
Silica	0	0	100				
SLS-71.9	14.1	14.1	71.9				
SLS-73.3[a]	14.9	11.8	73.3				
SLS-75.0[b]	12.5	12.5	75.0	SLS-71.9	Silica	4	12.0
SLS-75.3	12.3	12.4	75.3	SLS-75.0	Silica	2	1.5
SLS-76.2	11.9	11.9	76.2	SLS-75.0	Silica	3	5.0
SLS-77.7	11.1	11.2	77.7	SLS-75.0	Silica	4	12.0

[a]The SLS-73.3 system was only used for validation of the SLS glass structures obtained with the used simulation procedure by comparison with experimental neutron diffraction data [36] for a glass of this exact composition.
[b]The actual average composition of the phase-separated SLS-75.0 glass is $12.5Na_2O$–$12.6CaO$–$74.9SiO_2$ as the compositions of the SLS-71.9 glass cutouts differ slightly from the average composition due to the random distribution of the atoms.

followed by homogenization in the NPT ensemble for 2000 ps at 4700 K. The system was then cooled to 300 K at a cooling rate of 1 K/ps and relaxed at 300 K for 1000 ps in the NPT ensemble. For the SLS-71.9 and SLS-73.3 glasses, a pressure of 50 MPa was applied during the homogenization at 4700 K to avoid uncontrolled expansion of the simulation box, and the pressure was gradually released to zero during the cooling from 4700 to 4500 K.

We then combined the silica and SLS glasses to create four models of phase-separated glasses. By including a spherical silica droplet of diameter (D) 2, 3, or 4 nm into the SLS-75.0 glass structure, we obtained the phase-separated SLS-75.3, SLS-76.2, and SLS-77.7 glasses, respectively. The inclusion of a 4-nm silica droplet into the SLS-71.9 glass structure gave rise to the phase-separated SLS-75.0 glass, which has nearly the same average composition as the homogeneous SLS-75.0 glass. The compositions of all glasses can be found in Table I.

We followed the approach of Urata *et al.* [37] when combining the glass structures as described in detail in the following. First, a sphere ($D = 2,\ 3$, or 4 nm) was extracted from the silica glass. All silicon atoms within D were extracted, while the cutoff diameter for oxygen was adjusted to retain the composition (SiO_2) in the spherical cutout. A cavity was created in the cubic SLS glass structure (side length of 6.6 nm) by removing a sphere of diameter $D + 0.26$ nm. The radius of the cavity was made 0.13 nm larger than the silica sphere to avoid placing atoms in too close proximity to each other when combining the structures. To ensure charge balance, the cutoff diameter for sodium was adjusted to remove an even number of sodium atoms, and the cutoff diameter for oxygen was adjusted to ensure that the number of removed oxygen atoms matched the number of removed cations. The spherical silica cutout was then inserted into the cavity in the SLS glass. The combined structure was subjected to an energy minimization and then annealed at 1000 K for 500 ps in the NPT ensemble to ensure proper fusion of the two glass phases. The structure was then cooled to 300 K at 1 K/ps and relaxed at 300 K for 1000 ps in the NPT ensemble. Afterward, we produced homogeneous glass structures of the SLS-75.3, SLS-76.2, and SLS-77.7 systems. The glass formation procedure was identical to the melt-quench procedure described above, with the use of the phase-separated glasses as the initial structures instead of the randomly created configurations.

To investigate the effect of cooling rate on the glass structure, we prepared homogeneous SLS-75.0 and silica glasses using cooling rates of 100, 10, 0.1, and 0.01 K/ps following the same procedure as described above. Due to the computational cost of using lower cooling rates, only two repetitions were made of the glasses quenched at cooling rates of 0.1 and 0.01 K/ps and the system size of the glasses quenched at 0.01 K/s was reduced to approximately 4000 atoms. These glasses of different cooling rates were only used for structural characterization. Similarly, the finite-size effect was examined by preparing homogeneous SLS-75.0 and silica glasses of different system sizes and investigating their mechanical properties. Systems of approximately 2500, 5000, and 10 000 initial atoms were simulated in addition to the previously described system size of 20 000 atoms.

C. Structural characterization

To characterize the local structure around the silicon atoms, the silicon coordination number and Q^n distributions were calculated. The coordination number of each silicon atom was computed as the number of oxygen atoms within the first coordination shell (using a cutoff of 2.25 Å [26]), thus the silicon atom can be considered bonded to these oxygen atoms. The oxygen atoms are so-called bridging oxygens if they form bridges in the glass network by bonding to two silicon atoms (i.e., having two silicon atoms within a radius of 2.25 Å). The silicon atoms can be characterized as different Q^n units, where n denotes the number of bridging oxygens bonded to each silicon atom. Here, the numbers of the different Q^n units were computed to determine the Q^n distribution.

The neutron radial distribution function $g_N(r)$ and neutron structure factor $S_N(q)$ were computed for the homogeneous SLS-73.3, SLS-75.0, and silica glasses obtained by MD simulations to evaluate the structures and compare them with

experimental neutron diffraction data. Statistical averaging was achieved by simulating each glass structure in the NVT ensemble for 100 ps, from which 10 structures (60 structures in total due to the six repetitions) were sampled for computation of the partial radial distribution functions $g_{ij}(r)$. The $g_{\mathrm{N}}(r)$ function was then computed from the $g_{ij}(r)$ functions as

$$g_{\mathrm{N}}(r) = \frac{\sum_{i,j=1}^{n} c_i\, c_j\, \overline{b_i}\, \overline{b_j}\, g_{ij}(r)}{\sum_{i,j=1}^{n} c_i\, c_j\, \overline{b_i}\, \overline{b_j}}, \tag{1}$$

where c is the atomic fraction and $\bar{b}$ is the coherent bound neutron scattering length (5.803, 4.1491, 3.63, and 4.70 fm for oxygen, silicon, sodium, and calcium, respectively [38]). The $g_{\mathrm{N}}(r)$ functions obtained from simulations were broadened to enable meaningful comparison with experimental data, as the experimental $g_{\mathrm{N}}(r)$ functions are broadened due to the finite maximum momentum transfer in the experiments [39]. The $g_{\mathrm{N}}(r)$ functions from simulations were broadened by convolution with a Gaussian function with a full width at half maximum of $5.437/q_{\max}$, where $q_{\max}$ is the highest recorded momentum transfer of the experiments that have yielded the experimental $g_{\mathrm{N}}(r)$ functions used for comparison [40] ($q_{\max} = 15.4$ Å^{-1} for the SLS glasses [36] and $q_{\max} = 45.2$ Å^{-1} for the silica glass [41]). The R_χ factor introduced by Wright [39],

$$R_\chi = \sqrt{\frac{\sum_{i=1}^{n} \left(g_{\mathrm{N,exp}}(r_i) - g_{\mathrm{N,sim}}(r_i)\right)^2}{\sum_{i=1}^{n} \left(g_{\mathrm{N,exp}}(r_i)\right)^2}}, \tag{2}$$

was calculated to evaluate the agreement between the simulated and experimental $g_{\mathrm{N}}(r)$ functions. To avoid an effect from the ripples at low r values in the experimental data, only the data from the start of the first peak to 10 Å were used in the calculation of R_χ.

The partial structure factors $S_{ij}(q)$ were computed from the Fourier transforms of the $g_{ij}(r)$ functions,

$$S_{ij}(q) = 1 + \rho_0 \int_0^{r_{\max}} 4\pi\, r^2\, (g_{ij}(r) - 1) \frac{\sin(q\, r)}{q\, r} \frac{\sin\left(\frac{\pi\, r}{r_{\max}}\right)}{\frac{\pi\, r}{r_{\max}}}\, \mathrm{d}r, \tag{3}$$

where ρ_0 is the average atomic number density [40]. The maximum value of integration ($r_{\max}$) was set to half of the simulation box side length due to the periodic boundary conditions. A Lorch-type window function, $\sin(\pi r/r_{\max})/(\pi r/r_{\max})$, was used to reduce the effect of the finite cutoff in the Fourier transform. The total neutron structure factor $S_{\mathrm{N}}(q)$ was then computed from the $S_{ij}(q)$ functions,

$$S_{\mathrm{N}}(q) = \frac{\sum_{i,j=1}^{n} c_i\, c_j\, \overline{b_i}\, \overline{b_j}\, S_{ij}(q)}{\sum_{i,j=1}^{n} c_i\, c_j\, \overline{b_i}\, \overline{b_j}}. \tag{4}$$

D. Mechanical characterization

After preparing the simulated glasses, we characterized their mechanical properties, i.e., elastic properties (Young's modulus E and Poisson's ratio υ) and fracture parameters (fracture energy G_{C} and fracture toughness K_{Ic}). The average chemical composition is constant when experimental phase separation occurs; thus, we compare phase-separated systems with their homogeneous counterparts of equal average composition. Therefore, we have characterized the mechanical properties of both the phase-separated glasses and their homogeneous counterparts as well as the homogeneous matrix and droplet phases to evaluate and understand the effect of phase separation on the mechanical properties.

First, the elastic properties were determined. To avoid any contribution from thermal fluctuations, the elastic properties were examined at 0 K. Thus, the glass structure was first cooled to 0 K at a cooling rate of 1 K/ps in the NPT ensemble. The cubic structure was then subjected to tensile deformation by straining the box in increment steps of size $\Delta\varepsilon = 0.05\%$ until a total strain of $\varepsilon = 4\%$ was reached. Initially, and after each deformation, the structure was subjected to an energy minimization and the stress tensor was recorded. The structure was subjected to tensile deformation in the three spatial directions perpendicular to the box surfaces. The nine elastic stiffness constants for tensile deformation C_{11}, C_{12}, C_{13}, C_{21}, C_{22}, C_{23}, C_{31}, C_{32}, and C_{33} were determined as the slope of the appropriate stress-strain curves. Due to the isotropy of the homogeneous glasses and the rotational symmetry of the phase-separated glasses, the constants were averaged as $C_{11} = (C_{11} + C_{22} + C_{33})/3$ and $C_{12} = (C_{12} + C_{13} + C_{21} + C_{23} + C_{31} + C_{32})/6$. Following the same procedure, the structure was subjected to shear deformations to obtain the C_{44}, C_{55}, and C_{66} elastic stiffness constants, which were then averaged to obtain $C_{44} = (C_{44} + C_{55} + C_{66})/3$. Young's modulus and Poisson's ratio were calculated as [42,43]

$$E = \frac{(C_{11} - C_{12})(C_{11} + 2C_{12})}{C_{11} + C_{12}}, \tag{5}$$

$$\upsilon = \frac{C_{12}}{C_{11} + C_{12}}. \tag{6}$$

These equations for E and υ are valid for deformation in all directions of the homogeneous glasses due to their isotropy, while they are valid for deformation along the principal axes for the phase-separated glasses. However, the phase-separated glasses are nearly elastically isotropic, as their elastic anisotropy factor [43], i.e., $Z = 2C_{44}/(C_{11} - C_{12})$, are close to unity (we found $Z = 1.01 \pm 0.02$, where $Z = 1$ would indicate an elastically isotropic system). For this reason, the E and υ values calculated from Eqs. (5) and (6), respectively, are used for both homogeneous and phase-separated glasses.

Second, the fracture behavior of precracked glass samples was simulated, following the procedure of Brochard *et al.* [44]. This method has successfully been used to investigate the fracture properties and estimate fracture toughness of various silicate glasses [45–47] and other materials [48–50] using both reactive and fully classical potentials. The simulated structure, either homogeneous or phase-separated glass, was replicated into a $2 \times 2 \times 1$ supercell of approximately 80 000 atoms (box size of approximately $13.2 \times 13.2 \times 6.6$ nm^3). A precrack was introduced by removing atoms within the volume of an elliptic cylinder that was orientated with the elliptical cross section parallel to the largest faces of the supercell. For the phase-separated glasses, different positions of the crack relative to the particles were used as described

in Sec. III D. Charge neutrality was retained as previously described for the creation of the spherical cavity in the SLS glasses. The width of the ellipse was set to 25% of the simulation box side length (approximately 3.3 nm) to ensure that the crack was large enough to be stable but still accounted for only a small fraction of the cross section. To ensure stress concentration at the crack tips, the height of the ellipse was set to 20% of its width (approximately 0.66 nm). The precracked structure was relaxed by performing an energy minimization, followed by 1000 ps of relaxation at 300 K in the NPT ensemble. This was done while allowing the three box side lengths to vary independently and thus enable the normal stress tensor components for each spatial direction to relax toward 0. Finally, a 100-ps relaxation was performed in the NVT ensemble. During the relaxation, the introduced crack became slightly narrower and a small number of atoms entered the crack. Importantly, this did not result in closure of the crack as the crack was still clearly present with an almost unaffected shape, thus enabling the desired stress concentration at the crack tips.

To induce crack propagation and fracture, the precracked structure was then subjected to stepwise elongation of the simulation box perpendicular to the crack. A strain step size of $\Delta\varepsilon = 1\%$ was used, and the structure was elongated until a complete fracture of the glass was observed. Initially and after each deformation step, the structure was relaxed for 50 ps, followed by another 50 ps used for statistical averaging of the stress tensor. The fracture simulation was performed in the NVT ensemble at a temperature of 300 K. The strain rate was found to be slow enough to ensure convergence in the stress tensor components during the relaxation at each deformation step, enabling an accurate measurement of the stress required to deform the glass structure. The recorded stress in the deformation direction (σ_y) was used to plot the stress-strain curve associated with the fracture simulation. Integration of the stress-strain curve yielded the fracture energy (i.e., the critical energy release rate) by

$$G_C = \frac{L_x L_z}{\Delta A_\infty} \int_{L_{y,0}}^{L_{y,\max}} \sigma_y \, dL_y, \tag{7}$$

where L_x, L_y, and L_z are the dimensions of the simulation box along the x, y, and z directions and ΔA_∞ is the crack surface area formed during fracture [51]. Fracture toughness was then calculated using the Irwin formula in plane strain,

$$K_{Ic} = \sqrt{\frac{G_C E}{1-\nu^2}}. \tag{8}$$

The six repetitions yielded slightly different values of G_C and K_{Ic} for the same glasses, and we therefore performed two-sample t tests [52] to assess whether phase separation increases G_C and K_{Ic}. Specifically, the phase-separated glasses were compared one by one to their homogeneous counterparts of equal composition (hence, accounting for the effect of compositional variation). The null hypothesis was that the mean value of G_C (or K_{Ic}) is not different between phase-separated and homogeneous samples or that the homogeneous glass has the highest mean G_C (or K_{Ic}). Hence, the alternative hypothesis was that the mean G_C (or K_{Ic}) is highest for the phase-separated glass. A significance level of 0.05 was used.

The fracture energy G_C can be divided into two contributions: (i) surface energy, γ_s, and (ii) dissipated energy, G_{diss}, as the three energies are related through $G_C = 2\gamma_s + G_{diss}$. To quantify the brittleness of the investigated systems, we calculated the brittleness index, $B = 2\gamma_s/G_C$ [50]. The surface energy was calculated from the difference in potential energy between the precracked glass structure prior to fracture and the final structure after full fracture [37]. The potential energy was averaged over the 50 ps used for statistical averaging as described previously. The difference in potential energy was then divided by the area of the created surface, ΔA_∞, to obtain the surface energy, γ_s.

Finally, to investigate the buildup of stress locally in the structures during deformation, the per-atom stress tensors were computed during the fracture simulations. After each deformation step and subsequent relaxation, we minimized the potential energy of the structure and then calculated the per-atom stress tensors. The per-atom stress tensor component in the tensile deformation direction was then used to create a plot of the local tensile stress. In the plane parallel to the elliptical cross section of the crack, 100×100 equally distanced points (separation of approximately 1.3 Å) were used as reference points for the calculation of the local stress. The average per-atom tensile stress of all atoms within a circle of radius 5 Å around each reference point was calculated (the position along the third dimension was not considered; hence, the average is calculated for the atoms within a cylindrical volume). The overlap of the circles caused smoothing of the resulting plots, which was found necessary to reduce the noise to an acceptable level while maintaining good resolution.

III. RESULTS AND DISCUSSION

A. Validation of simulated homogeneous glass structures

We first validate the simulated homogeneous glass structures by comparing simulated densities with experimental measurements. The densities of the homogeneous glass of composition $12.5Na_2O$–$12.5CaO$–$75.0SiO_2$ (SLS-75.0) and the pure SiO_2 (silica) glass are 2.421 ± 0.002 g/cm^3 and 2.262 ± 0.002 g/cm^3, respectively. This is in good agreement with the experimental densities of 2.484 g/cm^3 for an SLS glass of similar composition ($15Na_2O$–$10CaO$–$75SiO_2$) [53] and 2.20 g/cm^3 for silica glass [54,55]. Importantly, the simulations replicate the correct trend with the modifier-rich glass having the highest density. Next, we evaluate the short-range structure around the silicon atoms, as described by the coordination number and Q^n distributions (Tables S1 and S2 in the Supplemental Material [56]). For both the SLS-75.0 and silica glasses, the coordination number of silicon is almost exclusively 4 as expected; however, a few defects (<0.2%) with coordination numbers of 3 or 5 are observed. Accordingly, primarily Q^4 units are present in the silica glass, with only minor fractions (<0.4%) of other Q^n species present. On the other hand, Na_2O and CaO in the SLS glasses give rise to nonbridging oxygens, resulting in significant fractions of Q^3 (41%) and Q^2 (11%) units in the simulated SLS-75.0 glasses besides the remaining Q^4 units (47%).

We evaluate the structure of the simulated SLS glasses by comparing the neutron radial distribution functions $g_N(r)$

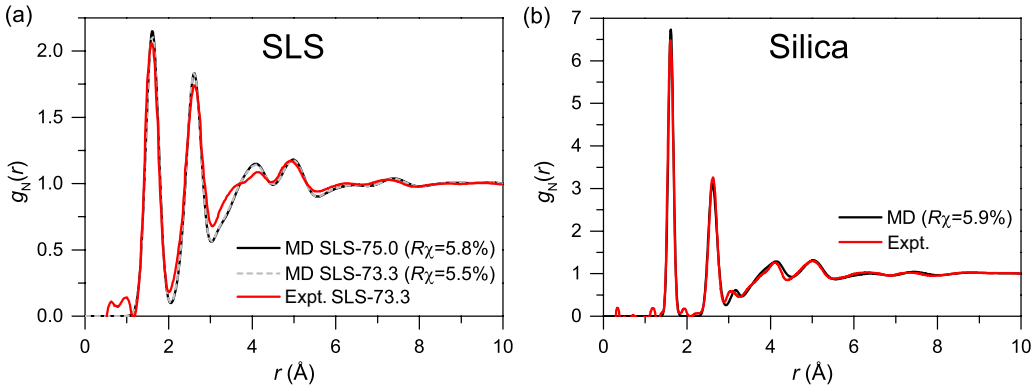

FIG. 1. Comparison of the neutron radial distribution functions $g_N(r)$ from the present MD simulations and experimental (Expt.) neutron diffraction data for homogeneous (a) soda-lime-silica and (b) silica glasses. Experimental data for a soda-lime-silica glass of composition $14.9Na_2O$–$11.8CaO$–$73.3SiO_2$ (SLS-73.3) are compared to a glass of identical composition and a glass of composition $12.5Na_2O$–$12.5CaO$–$75.0SiO_2$ (SLS-75.0). The experimental data were obtained from Refs. [36,41] and generally agree well with the simulated structures.

[Fig. 1(a)] and the neutron structure factors $S_N(q)$ [Fig. 2(a)] from simulations to experimental neutron diffraction data [36]. A glass of the SLS-73.3 composition (Table I) was used for the experimental study [36], and this is compared to a simulated glass of identical composition (SLS-73.3) and the simulated SLS-75.0 glass, generally showing very good agreement between the experimental and simulated results. The R_χ factor of 5.5% for the comparison of the $g_N(r)$ functions for the SLS-73.3 glass indicates a good replication of the experimental structure, although we note some discrepancies in $g_N(r)$ in the 3–4.5-Å range. The $g_N(r)$ function of the simulated SLS-75.0 glass is very similar to that of the simulated SLS-73.3 glass, yet it matches the experimental data slightly worse (R_χ factor of 5.8%) as expected due to the compositional difference. The neutron structure factors from simulations [Fig. 2(a)] show the same peaks as observed experimentally, but they fail to fully reproduce the exact peak positions and intensities. Comparison of the simulated and experimental [41] neutron radial distribution function for the silica glass [Fig. 1(b)] shows excellent agreement. The peak positions and intensities are well reproduced, although the peaks in the simulated data are shifted to slightly lower r values in the 3–4.5-Å range. The obtained R_χ factor of 5.9% verifies the good match between the experimental and simulated structure. The experimental and simulated neutron structure factors for the silica glass are very similar [Fig. 2(b)], especially at high q values, indicating very good replication of the short-range structure.

We have also investigated the effect of the simulated cooling rate on the structure of the SLS-75.0 and silica glasses (Figs. S1 and S2 in the Supplemental Material [56]). The cooling rate affects the structure as the peak intensities in the $g_N(r)$ and $S_N(q)$ functions vary, while the peak positions appear to be unaffected. Lowering the cooling rate gives better agreement with the experimental data for some peaks, while other peaks are less well reproduced. Thus, the use of a lower cooling rate that is closer to experimental rates does not significantly improve the agreement with the experimental data.

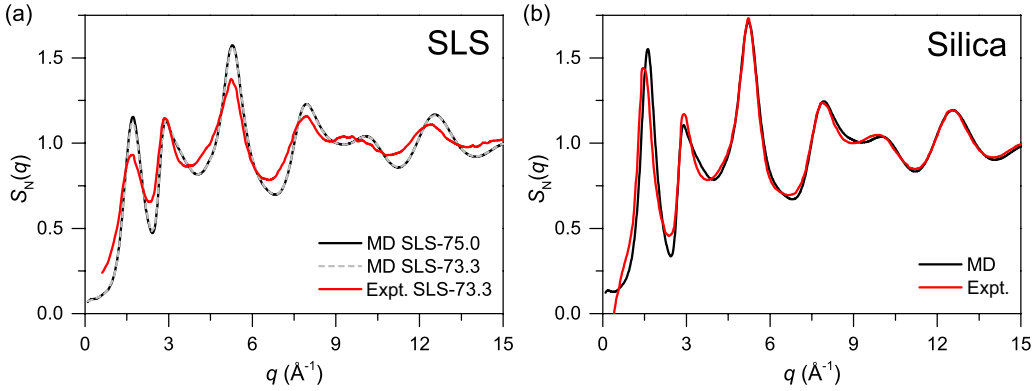

FIG. 2. Comparison of the neutron structure factors $S_N(q)$ from the present MD simulations and experimental (Expt.) [36,41] neutron diffraction data for homogeneous (a) soda-lime-silica and (b) silica glasses. Experimental data for a soda-lime-silica glass of composition $14.9Na_2O$–$11.8CaO$–$73.3SiO_2$ (SLS-73.3) are compared to a glass of identical composition and a glass of composition $12.5Na_2O$–$12.5CaO$–$75.0SiO_2$ (SLS-75.0). The simulated data for the silica glass agree very well with the experimental data, while the simulated data for the soda-lime-silica glasses show some differences with respect to the peak intensities, but the correct peaks are observed at the expected positions.

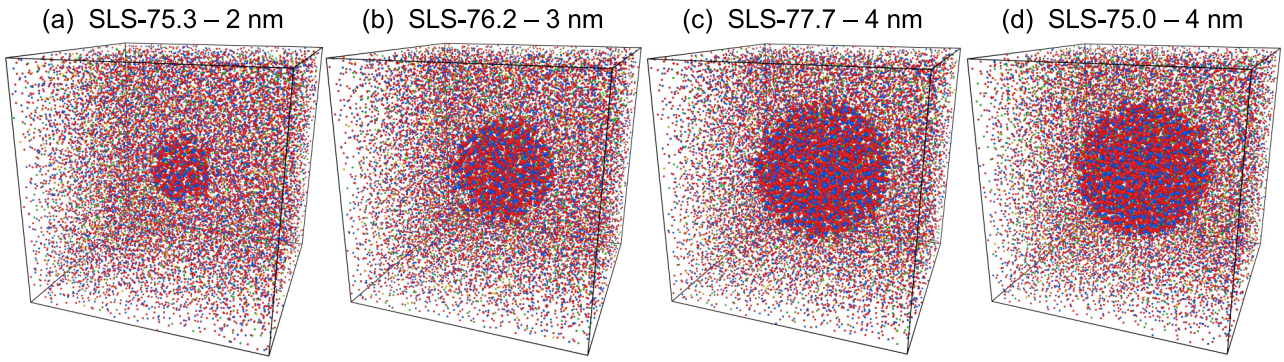

FIG. 3. Simulated structures of phase-separated soda-lime-silica glasses with silica inclusions. The SLS-75.3 (a), SLS-76.2 (b), SLS-77.7 (c), and SLS-75.0 (d) glass systems contain silica droplets of diameters 2, 3, 4, and 4 nm, respectively, corresponding to volume fractions of the silica phase of 1.5, 5.0, 12.0, and 12.0%, respectively (see details in Table I). The colors of the atoms represent the atom type (red is oxygen, blue is silicon, green is sodium, and yellow is calcium) and we note that the atoms within the silica droplets are enlarged for clarity.

Overall, the glass structures from MD simulations of both SLS and silica glasses generally match the experimental diffraction data, suggesting that the utilized potential and simulation procedure yield glasses with realistic structures.

B. Phase-separated glasses

To assess the effect of phase separation on mechanical properties, we have simulated four phase-separated SLS glasses with spherical silica nanodroplets of varying sizes (Fig. 3 and Table I). During the annealing following the merging of the two glass phases, structural rearrangements occur at the interface between the two phases. The unrealistic local atomic structures that exist prior to annealing in the interface region are removed, as the final glass consists of almost exclusively (>99.9%) fourfold coordinated silicon atoms. As some diffusion of sodium and calcium atoms occurs, we have quantified the compositional variation in the phase-separated glasses (Fig. S3 in the Supplemental Material [56]). We observe that the center of the particles is pure silica and the SLS matrix retains its composition, while a transition region is formed in between. In this interface, sodium, and to a lower extent calcium, diffuse into the silica phase, resulting in a compositional gradient over approximately 0.5 nm. We note that experimental phase separation in SLS glasses results in droplets of almost, but not completely, pure silica [17,57]; thus, some diffusion of sodium and calcium is acceptable. We note that the densities of the phase-separated glasses after annealing and subsequent quenching are slightly higher than those of the homogeneous glasses of equal average composition [Fig. 4(a) and Table II], indicating proper removal of the narrow void between the particle and matrix that was introduced during the preparation procedure.

It should be noted that the coefficient of thermal expansion (CTE) is different for the two phases in the phase-separated glasses. This can lead to internal residual stresses during cooling in both experiments and simulations, as internal stresses can only relax at high temperatures, while not at lower temperatures. The CTE of silica glass is lower than that of SLS glass [24], which is also observed in our simulations when quenching the homogeneous glasses; thus, the internal stresses can put the silica droplets under compression and the matrix under

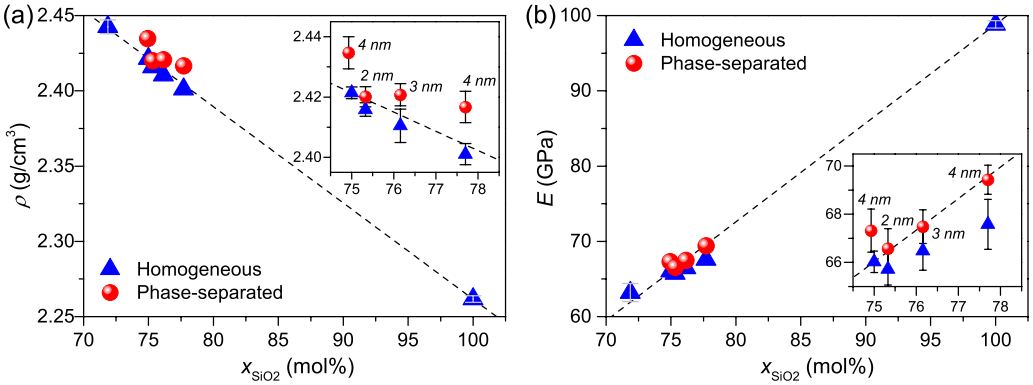

FIG. 4. Compositional dependence of (a) density ρ and (b) Young's modulus E. $x_{\mathrm{Si\,O2}}$ is the mole percentage of silica, i.e., the average compositions of the glasses are $(50 - x_{\mathrm{SiO_2}}/2)\mathrm{Na_2O}$–$(50 - x_{\mathrm{SiO_2}}/2)\mathrm{CaO}$–$x_{\mathrm{SiO_2}}\mathrm{SiO_2}$. The insets show enlarged views in the 75–78 mol % silica range. The red circles and blue triangles represent the phase-separated and homogeneous glasses, respectively, where the droplet diameters are indicated for the phase-separated glasses in the insets. The error bars represent the standard deviation, and the error bars for each point are shown once, either in the inset or the full plot. The dashed lines represent the linear fits between the data points of the homogeneous SLS-75.0 and silica glasses.

TABLE II. Density (ρ), Young's modulus (E), and Poisson's ratio (ν) for the homogeneous and phase-separated glasses (see details of the glass systems in Table I). The droplet diameter (D_{droplet}) is indicated for the phase-separated systems. The average standard deviation for ρ, E, and ν are found to be 0.003 g/cm^3, 0.7 GPa, and 0.003, respectively.

	Homogeneous glasses			Phase-separated glasses			
Glass ID	ρ (g/cm^3)	E (GPa)	ν (–)	D_{droplet} (nm)	ρ (g/cm^3)	E (GPa)	ν (–)
SLS-71.9	2.443	63.2	0.238				
SLS-75.0	2.421	66.0	0.231	4	2.435	67.3	0.238
SLS-75.3	2.416	65.7	0.228	2	2.420	66.6	0.233
SLS-76.2	2.410	66.5	0.229	3	2.421	67.5	0.235
SLS-77.7	2.401	67.6	0.228	4	2.417	69.4	0.233
Silica	2.262	98.8	0.217				

tension. Such internal residual stresses can cause microcracking in glass ceramics and thus affect fracture toughness [58], and this is also expected to be relevant for phase-separated glasses. Microcrack toughening increases fracture toughness; however, internal residual stresses can also have no or a negative effect on fracture toughness for glass ceramics [59,60]. In the analysis of the local stress (Sec. III D 3), we have not observed differences in the local stress in relation to the droplets before straining the structure (see Fig. S4 in the Supplemental Material [56]). As such, we do not consider this effect further in the current study.

C. Elastic properties

Before assessing the fracture dynamics of the glass systems, we focus on the elastic properties of the simulated glasses. Hence, we also evaluate the ability of the chosen MD potential to describe the mechanical properties. Specifically, Young's modulus (E) and Poisson's ratio (ν) have been estimated for the simulated glasses [Table II, Fig. 4(b), and Fig. S5 in the Supplemental Material [56]]. The simulated values for the homogeneous SLS-75.0 glass ($E = 66.0 \pm 0.4$ GPa and $\nu = 0.231 \pm 0.002$) are found to be in fair agreement with experimental data for a glass of similar composition ($E = 71.4$ GPa and $\nu = 0.22$, $15Na_2O$–$10CaO$–$75SiO_2$ [53]). However, some deviations are observed when comparing the experimental data for the silica glass ($E =$ 71.5–73.8 GPa and $\nu = 0.16$–0.176 [54,55,61]) with the simulated Young's modulus ($E = 98.8 \pm 0.5$ GPa) and Poisson's ratio (0.217 ± 0.002), i.e., the simulated silica glass shows higher Young's modulus and Poisson's ratio than observed experimentally. We note that the estimated Young's modulus and Poisson's ratio values for the phase-separated glasses are slightly higher than for the corresponding homogeneous glasses of equal average composition (see Fig. S6 in the Supplemental Material [56]).

D. Fracture toughness and crack propagation

In the following section, we focus on the fracture mechanics of the simulated homogeneous and phase-separated glasses, investigating how a preexisting crack propagates during tensile deformation. By replication of the four phase-separated glasses (see Table I and Fig. 3) into $2 \times 2 \times 1$ supercells and insertion of a precrack between two particles in each glass, we obtained precracked structures as shown in Figs. 5(a)–5(c). Due to the heterogeneity of the phase-separated glasses, the position of the precrack influences the crack propagation. We have thus investigated four different positions of the crack relative to the positions of the droplets for the system with 3-nm droplets, i.e., the SLS-76.2 glass (see crack positions A, B, C, and D in Fig. 5).

Tensile deformation of all precracked glasses (homogeneous or phase separated) has been simulated to investigate their fracture properties. When stretching a glass by forced elongation of the simulation box, the glass first deforms elastically without crack propagation. At higher strains, the crack starts to propagate as atomic rearrangements occur near the crack tips, leading to widening of the crack. Such limited crack propagation can be seen in Figs. 6(a) and 6(d) for strains of 13%. This is followed by a sudden fracture that divides the glass into two pieces, although a few atomic bridges between the fracture surfaces remain. Such atomic bridging has previously been observed during simulated fracture of silica glass [62] and other silicate glasses [45]. Snapshots of the structures during deformation are shown in Fig. 6 and more examples can be found in Figs. S7–S10 in the Supplemental Material [56].

The stress is measured to obtain stress-strain curves (Fig. 7) for the tensile deformation of the precracked glasses. The initial elastic deformation leads to a fairly linear rise in the stress until the yield point is reached, at which the stress levels off and then slightly decreases due to plastic deformation and limited crack propagation. A sudden drop in the stress is observed when the glass fractures, and the low-stress tail reaches zero when the atomic bridges break at higher strains. The glasses generally experience brittle fracture due to the sudden fracture and stress decrease, although some degree of nanoductility is observed from the structural rearrangements before fracture and the later formed atomic bridges. Nonetheless, we use the term fracture strain to describe the strain at which the stress rapidly decreases due to fracture. The fracture energies have been computed by integration of the stress-strain curves (see Computational Methods) and the fracture toughness of the various glass system have been calculated (Table III).

1. Homogeneous glasses

First, one may note how the fracture behavior of the homogeneous SLS and silica glasses varies significantly.

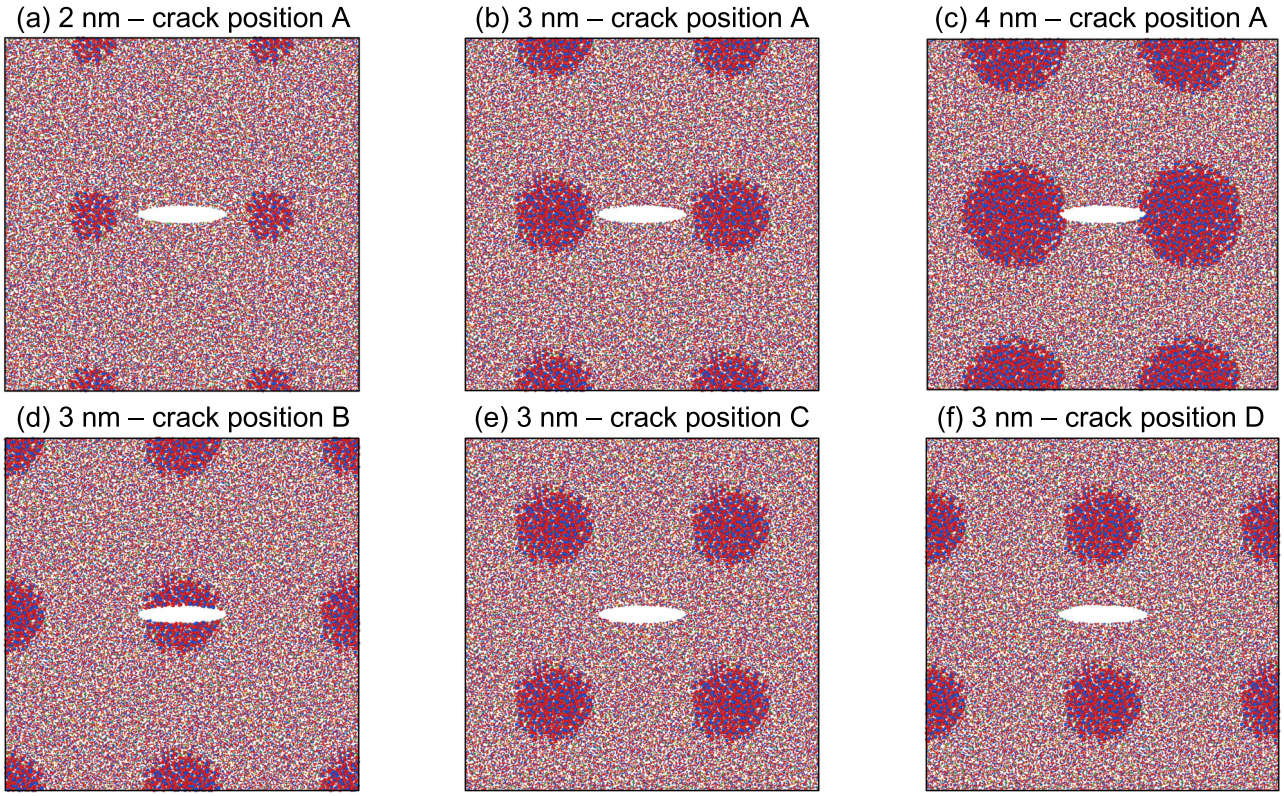

FIG. 5. Atomic configurations of the different structures (each with approximately 80 000 atoms) before being subjected to fracture simulations. The droplet size (diameters of 2, 3, and 4 nm) and position of the precrack relative to the droplets (crack positions A, B, C, and D) have been varied to investigate the effects hereof on crack propagation and fracture toughness. Two glasses containing 4-nm droplets (SLS-75.0 and SLS-77.7; see details in Table I) have been investigated using crack position A since the composition of their matrix phases differs, but only the structure of a phase-separated SLS-77.7 glass is shown (subfigure c). The atoms in the silica droplets are enlarged and the colors represent the atom type (red is oxygen, blue is silicon, green is sodium, and yellow is calcium).

The silica glass has the steepest stress increase (Fig. 7, gray curve) due to its higher elastic moduli, which causes the silica glass to reach higher maximum stress before fracture, showing that the silica glass is the strongest. The initial steepness of the stress-strain curve and the maximum stress decreases with increasing modifier content (Na_2O and CaO), while an increase in fracture strain is seen for increasing modifier content. Furthermore, the SLS glasses are more ductile at the nanoscale than the silica glass as their brittleness indexes (Table III) are lower, indicating a larger proportion of dissipated energy. The reported experimental fracture toughness (K_{Ic}) and fracture energy (G_C) of silica glass are 0.73–0.80 MPa $m^{1/2}$ and 8.8 J/m^2, respectively [4,63], while the simulations yield values of 0.89 ± 0.02 MPa $m^{1/2}$ and 7.9 ± 0.4 J/m^2, respectively. The overestimation of the fracture toughness is mainly caused by the overestimated Young's modulus, as mentioned previously. The estimated fracture toughness and fracture energy of the SLS-75.0 glass are $K_{Ic} = 0.69 \pm 0.03$ MPa $m^{1/2}$ and $G_C = 6.7 \pm 0.5$ J/m^2, respectively. To our knowledge, the fracture toughness of this glass has not been measured experimentally, but K_{Ic} values have been reported for similar SLS-type glasses, i.e., 0.67 MPa $m^{1/2}$ ($13Na_2O$–$0.4K_2O$–8.8CaO–4.3MgO–$0.6Al_2O_3$–$72.7SiO_2$), 0.70 MPa $m^{1/2}$ ($13.4Na_2O$–9.6CaO–4MgO–$0.6Al_2O_3$–$72SiO_2$), and 0.68–0.72 MPa $m^{1/2}$ ($13Na_2O$–10CaO–6MgO–$71SiO_2$) [4,64]. Noting the differences in composition, the simulated K_{Ic} values for SLS-75.0 and the other SLS glasses are in very good agreement with the experimental data.

The effect of the simulated system size on mechanical properties has been investigated for the homogeneous SLS-75.0 and silica glasses (Fig. S6 in the Supplemental Material [56]). Reducing the number of simulated atoms by a factor of 2, 4, or 8 does not significantly change the density, elastic properties, or fracture properties, although higher standard deviations are seen for the smaller system sizes, as expected. Thus, we find the used simulation procedure to be applicable and not depend on the system size in this range.

2. Effects of matrix composition and droplet size

Next, we focus on the effect of phase separation on the fracture behavior, starting with the systems of crack position A but of varying matrix compositions and droplet diameters. First, we note how the silica inclusions affect the fracture behavior of the glasses as seen from the fracture simulation snapshots and stress-strain curves in Figs. 6 and 7, respectively. More atomic snapshots are shown in Figs. S7–S10 in the Supplemental Material [56]. When the crack is located between two droplets (crack position A), it can be observed how the crack is arrested at the droplets when straining the structure. For the 4-nm droplet systems (SLS-75.0 and SLS-77.7)

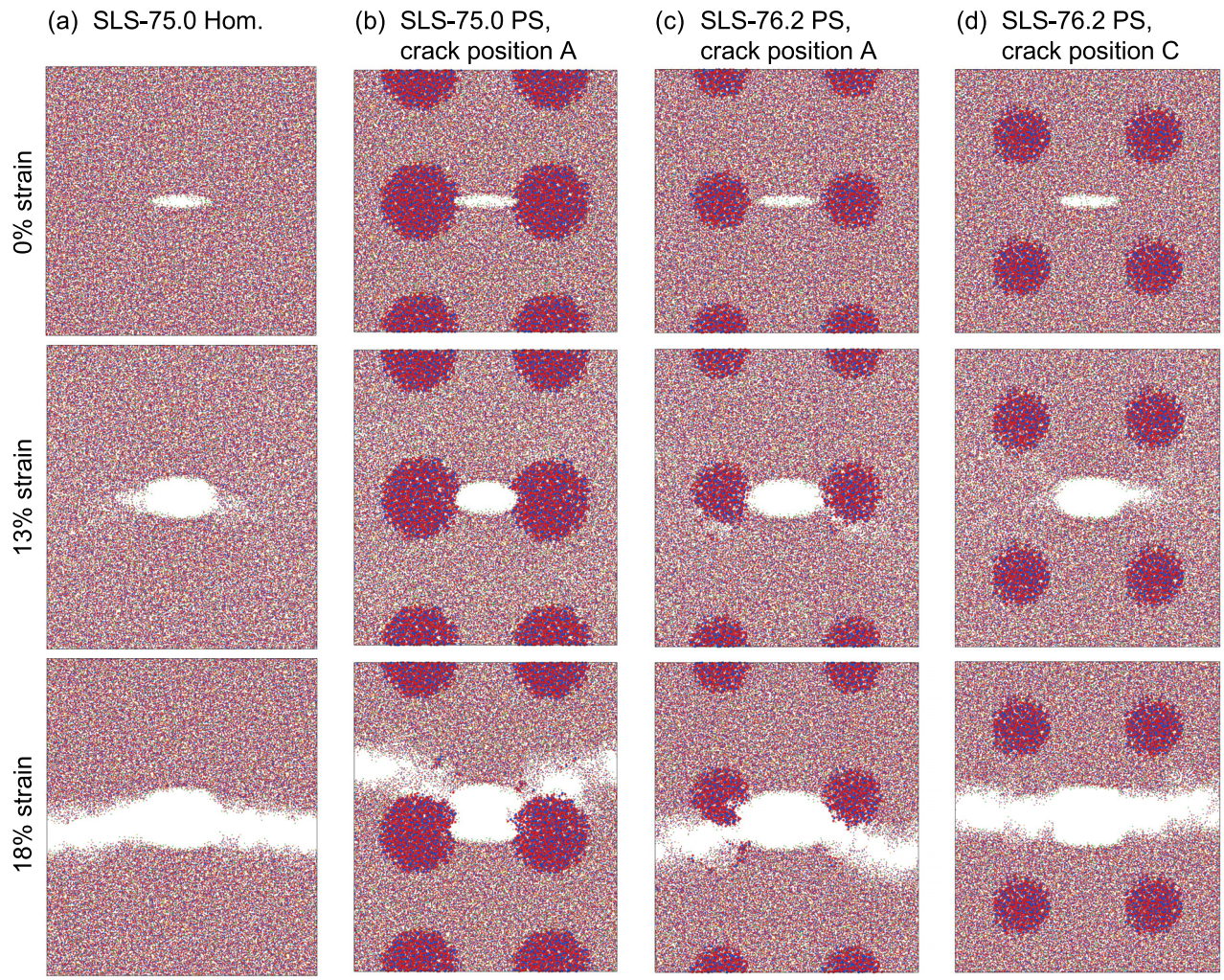

FIG. 6. Atomic configuration snapshots during fracture at different strain values for four exemplary glasses, namely (a) homogeneous (Hom.) soda-lime-silica glass of composition $12.5Na_2O$–$12.5CaO$–$75.0SiO_2$ (SLS-75.0), (b) phase-separated (PS) SLS-75.0 glass with 4-nm droplets and crack position A, (c) phase-separated SLS glass of composition $11.9Na_2O$–$11.9CaO$–$76.2SiO_2$ (SLS-76.2) with 3-nm droplets and crack position A, and (d) phase-separated SLS-76.2 glass with 3-nm droplets and crack position C. The crack positions are illustrated in Fig. 5. The top row shows the elliptical precracks of their original shape at zero strain. First, the crack is opened without propagation of the crack until a strain of roughly 13%, at which the crack starts to propagate, and finally the glass experiences complete fracture. A few atomic bridges can be seen between the fracture surfaces and these break at higher strains. Atomic snapshots during fracture are shown in Figs. S7–S10 in the Supplemental Material [56] for all investigated homogeneous and phase-separated glasses.

where the crack tips are located at the droplets at zero strain, no crack propagation is observed at the strain values where it has initiated in the homogeneous glasses, i.e., crack arrest is observed (Figs. 6(a) and 6(b) and Figs. S8(c) and S9(d) in the Supplemental Material [56]). For the 3-nm droplet system (SLS-76.2) shown in Fig. 6(c), the crack can propagate a short distance through the SLS phase but is then arrested at the droplets. Following the crack arrest in all systems, the crack propagation continues at higher strain values and the glass eventually fractures. Here, the crack is either diverted around the droplets or alternatively traverses one or both of the droplets. The crack propagation traversing a droplet can either (i) divide the droplet into two parts of similar size or (ii) be deflected, resulting in the splitting of the droplet into two parts of significantly different sizes. As different crack propagation paths are seen for the six independent repetitions of each fracture simulation, we quantify how frequently the crack is either diverted or deflected at the particles. By visual examination of the fractured structures (see Fig. S11 in the Supplemental Material [56]), we find that the crack is either diverted or deflected at about 90, 60, 75, and 60% of the particles in the SLS-75.0, SLS-75.3, SLS-76.2, and SLS-77.7 glasses, respectively.

The effect of the presence of droplets on fracture is also reflected in the stress-strain curves. Figure 7(a) shows the stress-strain curves from the fracture simulations of the homogeneous and phase-separated SLS-75.0 glasses. Additionally, the stress-strain curves for the two glass phases (SLS-71.9 and silica) that are present in the phase-separated SLS-75.0 glass are shown. The stress-strain curve for the phase-separated SLS-75.0 glass initially follows that of the homogeneous SLS-75.0 glass, yet, the phase-separated glass reaches higher maximum stress and fractures at a higher strain, which we ascribe to the crack arrest and diversion/deflection phenomena

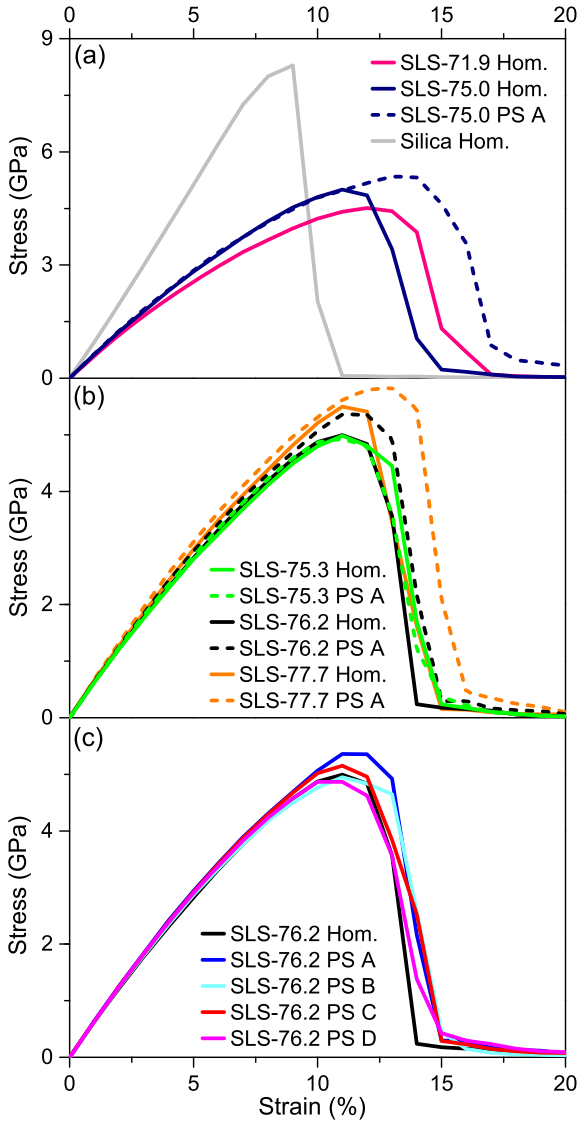

FIG. 7. Stress-strain curves from the fracture simulations of homogeneous and phase-separated glasses. The details of the different glasses are given in Table I, and the crack positions (A–D) for the phase-separated glasses are shown in Fig. 5. (a) Stress-strain curves for fracture of homogeneous and phase-separated SLS-75.0 glasses, as well as for the two phases of the phase-separated SLS-75.0 glass, i.e., SLS-71.9 and silica. (b) Stress-strain curves for the phase-separated glasses of identical matrix composition (SLS-75.0) and varying droplet sizes of 2, 3, and 4 nm for SLS-75.3, SLS-76.2, and SLS.77.7, respectively. The glasses were fractured using crack position A, i.e., the precrack was located between two droplets. Furthermore, the curves for the homogeneous glasses of identical average compositions are shown. (c) Stress-strain curves for the phase-separated SLS-76.2 glasses with 3-nm silica droplets for various positions of the crack, as well as for the homogeneous glass of identical average chemical composition.

described above. The larger area under the stress-strain curves upon phase separation leads to an increase in both the estimated G_C (14%) and K_{Ic} (8%) values (Table III and Fig. 8), thus showing toughening by nanoscale phase separation. Toughening by phase separation is also observed for the SLS-77.7 glass as seen from the G_C and K_{Ic} values (increased by 14 and 9%, respectively). The phase-separated SLS-77.7 glass is identical to the phase-separated SLS-75.0 glass except for the difference in matrix phase composition, and similar toughening mechanisms are observed as both of the phase-separated systems exhibit higher maximum stress and fracture strain than their homogeneous counterparts. We note that the difference in composition of the two phase-separated systems leads to generally higher G_C, K_{Ic}, and maximum stress values but lower fracture strain values for the more silica-rich SLS-77.7 system, similar to the observed trends for the homogeneous glasses (Sec. III D 1). We find it noticeable that the fracture strain values of both the phase-separated SLS-75.0 and SLS-77.7 glasses are higher than those of their homogeneous counterparts, their matrix phase glass, and their droplet phase glass. Thus, the compositional variation of the phases cannot explain the observed fracture strain increase, pointing towards the importance of the crack arrest mechanism.

We next consider the effect of particle size on fracture mechanics, which has been simulated for phase-separated glasses of constant matrix phase composition, i.e., SLS-75.3, SLS-76.2, and SLS-77.7. The initial slope of the stress-strain curves [Fig. 7(b)] increases with higher silica content, and the phase-separated glasses have slightly larger slopes than their homogeneous counterparts, all due to the variations in Young's modulus [Fig. 4(b)]. In addition to the effect on the elastic deformation, the presence of droplets in the phase-separated glasses also increases the fracture strain and maximum stress due to the observed crack arrest for the 3- and 4-nm droplet systems, ultimately toughening the systems. The effect is more pronounced for larger silica droplets, suggesting that these provide more effective crack arrest. The effects of phase separation on fracture mechanics for the 2-nm system (SLS-75.3) are relatively small, presumably because the small droplet size (∼285 atoms per droplet) causes less effective crack arrest. Indeed, the phase-separated 2-nm system features a lower fracture strain than its homogeneous counterpart, but this is compensated to some degree by the larger initial stress increase when evaluating the fracture toughness.

The estimated fracture energy and fracture toughness values for all phase-separated glasses with crack position A are given in Table III and Fig. 8, showing the more effective crack arrest by the droplets of larger size. The increase of K_{Ic} upon phase separation is not as pronounced as for G_C, illustrated by the 4-nm droplets systems having G_C values similar to that of pure silica, while their K_{Ic} values are significantly lower than that of silica. However, the increase in K_{Ic} for the phase-separated systems is significant according to the results of the t tests for the 3- and 4-nm systems (SLS-75.0, SLS-76.2, and SLS-77.7). Thus, we have shown that changes in the nanostructure of the SLS glass upon phase separation can improve the fracture properties. Furthermore, we note how the brittleness index values (Table III) for fracture of the phase-separated glasses are slightly lower than those for the homogeneous SLS glasses, indicating that the presence of the droplets increases the proportion of dissipated energy and hence the ductility.

It should be noted that the energy required to cause fracture increases more upon phase separation than that apparently seen from the G_C values in Fig. 8(a). The crack diversion

TABLE III. Fracture energy (G_C), fracture toughness (K_{Ic}), and brittleness index (B) for the homogeneous and phase-separated glasses (see details of the glass systems in Table I). Various relative positions of droplets and precrack for the fracture simulations have been investigated as indicated by crack positions A, B, C, and D (see Fig. 5). Furthermore, the droplet diameter ($D_{droplet}$) is indicated for the phase-separated systems. The average standard deviation for G_C, K_{Ic}, and B are found to be 0.4 J/m^2, 0.02 MPa m$^{1/2}$, and 0.01, respectively.

	Homogeneous glasses			Phase-separated glasses				
Glass ID	G_C (J/m^2)	K_{Ic} (MPa m$^{1/2}$)	B (–)	Crack position	$D_{droplet}$ (nm)	G_C (J/m^2)	K_{Ic} (MPa m$^{1/2}$)	B (–)
SLS-71.9	7.0	0.68	0.30					
SLS-75.0	6.7	0.69	0.32	A	4	7.7	0.74	0.30
SLS-75.3	6.8	0.69	0.32	A	2	6.8	0.69	0.31
SLS-76.2				A	3	7.3	0.72	0.31
SLS-76.2				B	3	7.0	0.71	0.31
SLS-76.2	6.6	0.68	0.33	C	3	7.2	0.72	0.31
SLS-76.2				D	3	6.7	0.69	0.32
SLS-77.7	7.0	0.71	0.32	A	4	8.0	0.77	0.31
Silica	7.9	0.90	0.43					

and deflection phenomena induce a larger number of broken bonds, increasing the energy needed to fracture the glass. However, this is not reflected in G_C due to the longer crack path, increasing the fracture surface area. As shown in Fig. 9, a larger increase in G_C, and hence also K_{Ic}, is observed when normalizing the energy by the cross-section area (corresponding to a perfectly flat fracture surface) instead of the actual rugged fracture surface area, ΔA_∞, in Eq. (7). This method is similar to the stress-strain curve integration approach in the work of Urata *et al.* [37], but here we have added a correction for the area initially split by the precrack. This alternative calculation includes the effect of crack diversion/deflection as it is not canceled by the area normalization, thus showing a greater effect of phase separation on the fracture energy and toughness.

3. *Effects of relative position of crack and droplets*

As we have just shown, the silica droplets can toughen the glasses by arresting, deflecting, and diverting the propagating cracks. It should thus be expected that the configuration where the crack is in between two droplets (crack position A) has the greatest impact on the crack propagation process, as the propagating crack will most rapidly encounter the droplets for this crack position. In the following, we investigate the crack propagation in SLS-76.2 glasses (droplet size of 3 nm) using different positions of the crack relative to the droplets. Atomic snapshots of the fracture simulations can be found in Fig. 6 and Figs. S8–S10 in the Supplemental Material [56]. For crack position B, where the crack is positioned inside a droplet, the crack propagates towards the single droplet in the crack path and is then either diverted around the droplet or traverses the droplet. For crack positions C and D, where there are no droplets in the crack propagation path, the crack opens and fractures the glass without any direct interaction with the droplets.

The stress-strain curves [Fig. 7(c)] show that for crack position A, both the maximum stress and fracture strain increase as compared to the homogeneous glass of identical composition. As previously described, this is also reflected

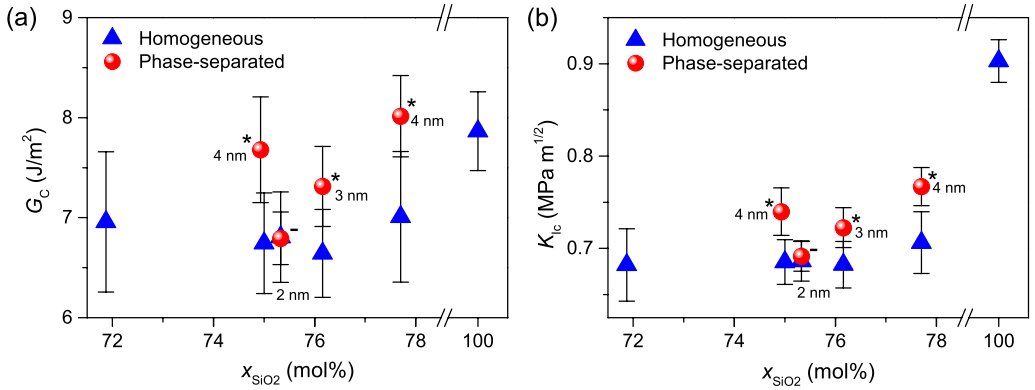

FIG. 8. (a) Fracture energy G_C and (b) fracture toughness K_{Ic} for systems with crack position A (see Fig. 5) and of varying average composition. $x_{Si\,O2}$ indicates the mole percentage of silica in the glass, i.e., the compositions are $(50 - x_{SiO_2}/2)Na_2O$–$(50 - x_{SiO_2}/2)CaO$–$x_{SiO_2}SiO_2$. The blue triangles represent the homogeneous glasses, and the red circles represent the phase-separated glasses where the number indicates the droplet diameter. The error bars represent the standard deviation, and the asterisks (*) indicate that the mean value for the phase-separated glass is higher than the mean for the homogeneous glass with the same average composition according to the t tests, whereas a minus sign (−) indicates that the null hypothesis was not rejected (see Sec. II D).

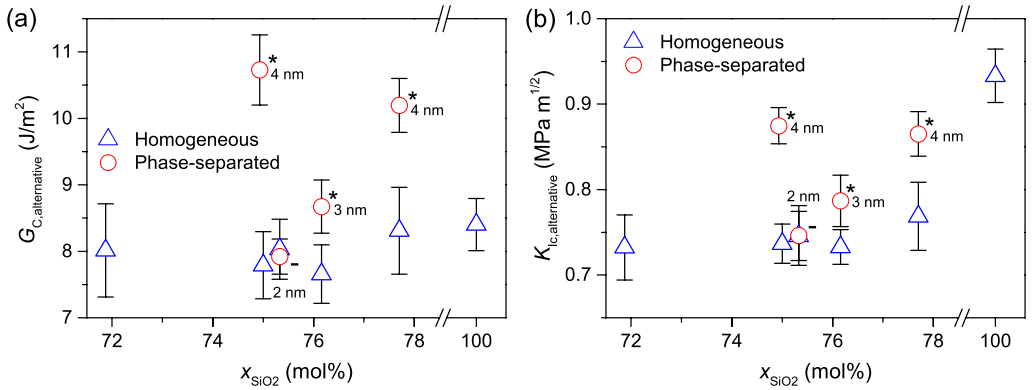

FIG. 9. (a) Fracture energy G_C and (b) fracture toughness K_{Ic} values calculated using an alternative area calculation relative to the results in Fig. 8, as we here use the area of a perfectly flat fracture surface as ΔA_∞ in Eq. (7). The values are shown for the homogeneous (blue triangles) and phase-separated (red circles) glasses fractured using crack position A (see Fig. 5). The error bars represent the standard deviation, and the asterisks (*) indicate that the mean value for the phase-separated glass is higher than the mean for the homogeneous glass with the same average composition according to the t tests, whereas a minus sign (−) indicates that the null hypothesis was not rejected (see Sec. II D).

in increased values of G_C and K_{Ic} (Fig. 10 and Table III). The silica droplets in the glass with crack position B cause the fracture strain to increase; however, the maximum stress is not significantly affected. This can be explained by initial propagation of the crack without direct interaction with the droplets; thus, the maximum stress is almost unchanged compared to the homogeneous glass. However, the crack reaches a droplet at a higher strain, impeding the propagation and thus causing the higher fracture strain. An increase in both G_C and K_{Ic} is seen for crack position B compared to the homogeneous glass (Fig. 10), but the increases are not significant according to the t tests.

The introduction of droplets that are not in the proximity of the crack tips and crack propagation path also affects the fracture behavior of the glasses, as investigated with crack positions C and D. Crack position C results in higher maximum stress and fracture strain compared to the homogeneous glass [Fig. 7(c)], with G_C and K_{Ic} values similar to those of crack position A (Fig. 10 and Table III). The toughening without direct crack-particle interactions suggests that an alternative mechanism besides crack arrest and diversion/deflection can induce toughening of the phase-separated glasses. On the other hand, no major effect of phase separation on any fracture parameters is observed for crack position D, despite minor differences in the stress-strain curve. The comparison of results for crack positions C and D points towards a possible explanation of the toughening effect, as differences in the stress field upon straining are observed due to the presence of two phases with different properties.

Therefore, we investigate the distribution of local stress during the fracture simulations in the following. The local average per-atom tensile stress along the direction of deformation is shown for the homogeneous SLS-76.2 glass at different strain values in Fig. 11. Minor local variations in the stress can be seen at zero strain, but tensile stress is then progressively built up when straining the structure to 5 and 10%. Stress concentration at the crack tips is observed and regions of lower tensile stress are seen near the faces of the crack [blue regions seen above and below the crack in Fig. 11(c)]. At 18% strain, the glass has experienced fracture and the stresses are thus

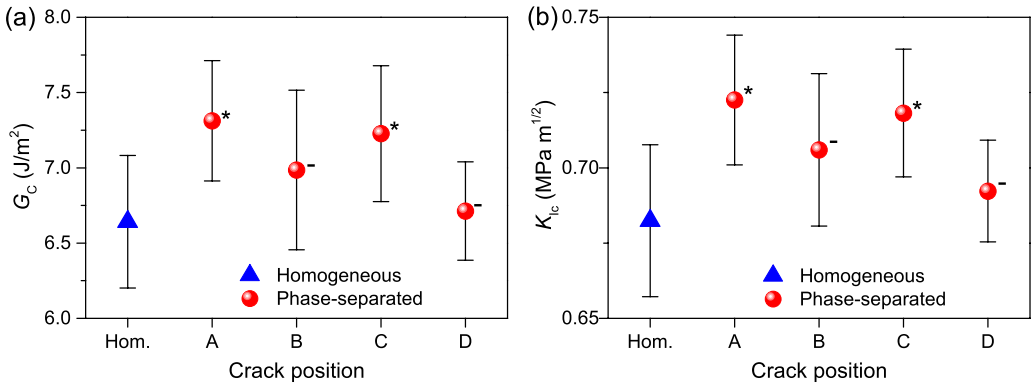

FIG. 10. Dependence of (a) fracture energy G_C and (b) fracture toughness K_{Ic} on the crack position (see Fig. 5) for the simulations of the SLS-76.2 glass ($11.9Na_2O$–$11.9CaO$–$76.2SiO_2$) containing droplets of 3-nm diameter. The red circles represent the phase-separated glasses, and the blue triangles represent the homogeneous glass with identical average composition. The error bars represent the standard deviation, and the asterisks (*) indicate that the mean value for the phase-separated glass is higher than the mean for the homogeneous glass according to the t tests, whereas a minus sign (−) indicates that the null hypothesis was not rejected (see Sec. II D).

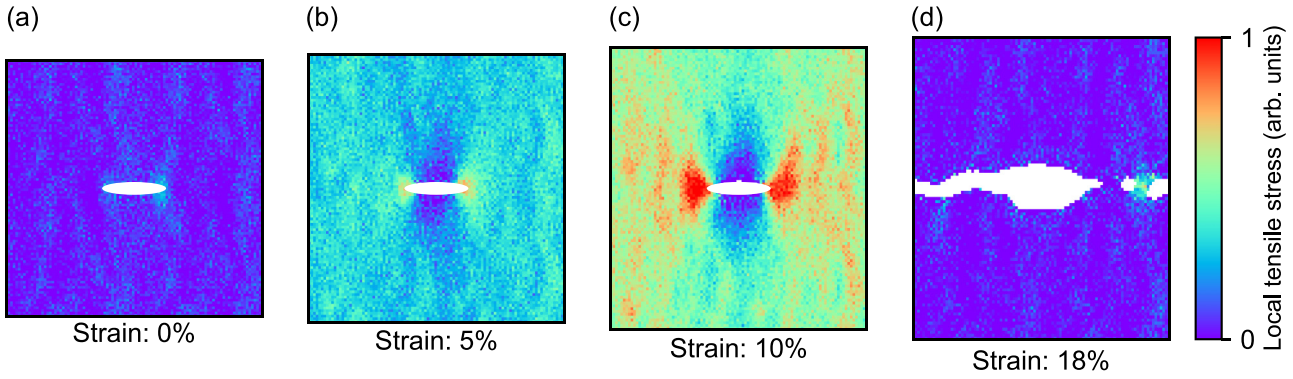

FIG. 11. Local average per-atom stress in the deformation direction in the homogeneous SLS-76.2 glass at different strain values. The tensile stress increases when the glass is strained (subfigures b and c) until fracture occurs at around 13% strain, after which significant stress levels are only present at atomic bridges between the two fracture surfaces (subfigure d). The white ellipse shows the initial position of the crack and the white pixels for 18% strain represent points where no or only a few atoms were located within the cylindrical volume used to calculate the average per-atom stress. The color scale represents the values in the range from zero stress to an arbitrarily chosen tensile stress (positive values), thus coloring values outside this range (including compressive stresses) as the endpoints of the scale. The same color scale is used for all subplots (a)–(d) as well as in Fig. 12.

again close to zero throughout the glass, except for the stress at the remaining atomic bridges. Figure 12 shows the local tensile stress for the phase-separated SLS-76.2 glasses (3-nm droplets) at a constant strain of 10%, i.e., prior to fracture for all structures. All these glasses exhibit stress concentration at the crack tips, similar to the homogeneous SLS-76.2 glass (Fig. 11). The illustration reveals how the droplets affect the stress field by forming new regions of high stress in addition to the stress at the crack tips, namely bands of high stress orientated along the deformation direction and overlapping with the droplets (seen as vertical bands of higher stress in Fig. 12). These bands are formed as a consequence of the higher Young's modulus of the silica droplets, and they can explain the difference in fracture behavior between crack positions C and D. Two droplets are located close to the crack faces for crack position D, thus promoting an opening of the crack due to the overlap of a high-stress band and the crack. This explains the slightly lowered maximum stress for crack position D [Fig. 7(c)], as the crack starts propagating at a lower strain. However, no overall effect on G_C and K_{Ic} is observed when comparing with the homogeneous glass. The lower maximum stress is compensated by a slower decline of the stress, which can be explained by the difference in the phase, in which the crack is propagating. The matrix phase of the phase-separated glass is more modifier rich than the homogeneous glass, leading to lower brittleness (Table III) and increased fracture strain [Figs. 7(a) and 7(b)] of this phase. For crack position C, the two stress bands caused by the droplets do not overlap with the crack; hence, the stress is built up around the crack. At the same time, the stress that contributes force to the opening of the crack is reduced compared to the homogeneous glass. This is due to the lower Young's modulus of the matrix phase, as a consequence of its higher modifier content [Fig. 4(b) and Table II]. These effects on the distribution of local stress lead to higher fracture energy and toughness for crack position C, as the crack is shielded from the stress in this system. This mechanism of altering the stress field provides an alternative toughening mechanism to

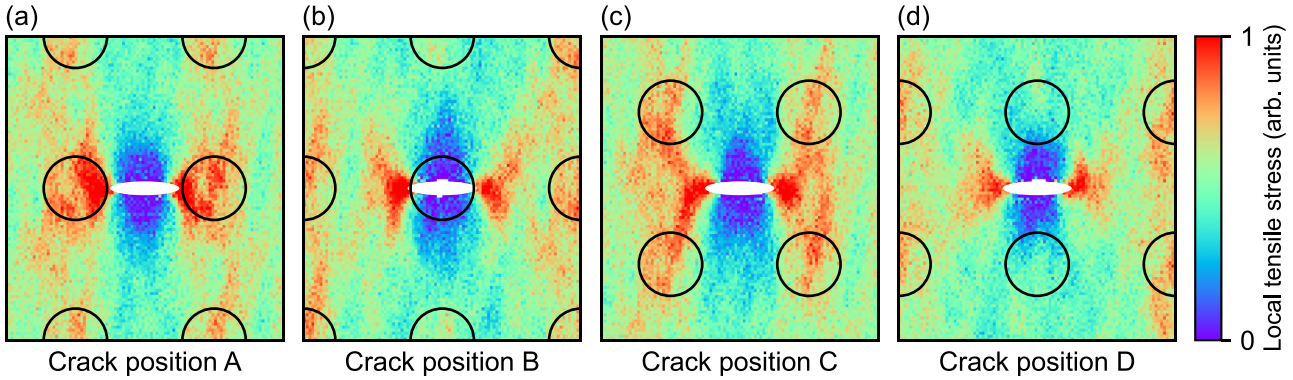

FIG. 12. Local average per-atom tensile stress at 10% strain (prior to fracture) of phase-separated SLS-76.2 glasses ($11.9Na_2O$–$11.9CaO$–$76.2SiO_2$) containing droplets of 3-nm diameter, but with varying crack position. The white ellipse shows the initial position of the crack and the black circles show the approximate positions of the silica droplets. The color scale represents the values in the range from zero stress to an arbitrarily chosen tensile stress (positive values), thus coloring values outside this range (including compressive stresses) as the endpoints of the scale. The same scale is used for all four subplots as well as in Fig. 11.

the one based on crack arrest, deflection, and diversion that is encountered when the droplets are in the direct vicinity of the crack path.

E. Implications for future experimental investigations

To the authors' knowledge, the effect of phase separation on fracture toughness has not been experimentally investigated for SLS glasses, but our findings encourage such studies of toughening by nanoscale droplet formation. We have found that the direct crack-particle interactions (crack arrest, deflection, and diversion) are considerably more efficient for larger particle sizes, suggesting that experimental studies should aim at maximizing the droplet size, yet keeping the droplets significantly smaller than the wavelength of visible light to retain transparency. Furthermore, the number of droplets should also be considered, as crack arrest events are more likely to occur for a larger number of particles. Thus, if the droplet size is increased due to a coarsening process that reduces the number of droplets, this might lead to a less effective toughening effect. Crack propagation was observed to preferably occur in the matrix phase of phase-separated SLS glasses, in agreement with the observations of Tang *et al.* [16] for droplets of higher stiffness. Thus, the matrix phase should preferably be optimized to be intrinsically tough, enhancing overall toughness. We note that the simulated droplet sizes (diameters of 2, 3, and 4 nm) are smaller than the droplets observed in an experimental study of phase separation in SLS glasses [17], although the size estimation in this study was limited by the microscope resolution. Formation of droplets with an average diameter of 25 nm was observed in a glass of the SLS-75.0 composition upon heat treatment at 640 °C for 1 h, yet heat treatments of shorter duration or lower temperature should form smaller droplets, approaching the droplet sizes investigated in this study.

IV. CONCLUSIONS

Using atomistic simulations, we have studied the fracture behavior of soda-lime-silica glasses with embedded glassy silica nanodroplets and demonstrated a toughening effect by the droplets. The investigated systems mimic the structure of phase-separated soda-lime-silica glasses, thus showing the potential of toughening glasses by nanoscale phase separation. The crack propagation path is affected by crack arrest, crack deflection, and crack diversion when a propagating crack in the soda-lime-silica glass matrix encounters a glassy silica droplet, increasing the fracture energy and fracture toughness of the phase-separated glasses. Other toughening effects have been described besides the direct crack-particle interaction, as the heterogeneous nanostructure of the phase-separated glasses results in a less brittle matrix and alterations of the stress field. An altered stress field has been demonstrated to induce toughening by allowing stress buildup around the crack without promoting the opening of the crack. However, the alteration of the stress can have the opposite effect for other relative positions of droplets and crack. Further work is required to understand the effect of this mechanism on the fracture toughness of phase-separated glasses with randomly distributed droplets.

The data supporting the results within this paper are available from the corresponding author upon reasonable request.

ACKNOWLEDGMENTS

This work was supported by VILLUM FONDEN under Research Grant No. 13253. The authors also thank Aalborg University for access to computational resources through CLAAUDIA. M.B. acknowledges funding from the National Science Foundation under Grant No. CMMI-1762292.

[1] L. Wondraczek, J. C. Mauro, J. Eckert, U. Kühn, J. Horbach, J. Deubener, and T. Rouxel, Towards ultrastrong glasses, Adv. Mater. **23**, 4578 (2011).

[2] R. O. Ritchie, The conflicts between strength and toughness, Nat. Mater. **10**, 817 (2011).

[3] E. D. Zanotto and F. A. B. Coutinho, How many non-crystalline solids can be made from all the elements of the periodic table? J. Non-Cryst. Solids **347**, 285 (2004).

[4] T. Rouxel and S. Yoshida, The fracture toughness of inorganic glasses, J. Am. Ceram. Soc. **100**, 4374 (2017).

[5] A. K. Varshneya, Chemical strengthening of glass: Lessons learned and yet to be learned, Int. J. Appl. Glass Sci. **1**, 131 (2010).

[6] A. K. Varshneya, Stronger glass products: Lessons learned and yet to be learned, Int. J. Appl. Glass Sci. **9**, 140 (2018).

[7] F. C. Serbena, I. Mathias, C. E. Foerster, and E. D. Zanotto, Crystallization toughening of a model glass-ceramic, Acta Mater. **86**, 216 (2015).

[8] M. Montazerian and E. D. Zanotto, Tough, strong, hard, and chemically durable enstatite-zirconia glass-ceramic, J. Am. Ceram. Soc. **103**, 5036 (2020).

[9] J. Moriceau, P. Houizot, T. To, A. Mougari, H. Orain, F. Celarié, and T. Rouxel, Nucleation and crystallization of $Ba_2Si_3O_8$ spherulites in a barium aluminum silicate glass, and mechanical properties of the obtained glass-ceramics, J. Eur. Ceram. Soc. **41**, 838 (2021).

[10] G. H. Beall and D. A. Duke, Transparent glass-ceramics, J. Mater. Sci. **4**, 340 (1969).

[11] M. Ono, S. Miyasaka, Y. Takato, S. Urata, H. Yoshino, R. Ando, and Y. Hayashi, Higher toughness of metal-nanoparticle-implanted sodalime silicate glass with increased ductility, Sci. Rep. **9**, 15387 (2019).

[12] N. Miyata and H. Jinno, Use of Vickers indentation method for evaluation of fracture toughness of phase-separated glasses, J. Non-Cryst. Solids **38-39**, 391 (1980).

[13] N. Soga, Elastic moduli and fracture toughness of glass, J. Non-Cryst. Solids **73**, 305 (1985).

[14] A. K. Seal, P. Chakraborti, N. R. Roy, S. Mukherjee, M. K. Mitra, and G. C. Das, Effect of phase separation on the fracture toughness of SiO_2-B_2O_3-Na_2O glass, Bull. Mater. Sci. **28**, 457 (2005).

[15] G. D. Quinn and R. C. Bradt, On the Vickers indentation fracture toughness test, J. Am. Ceram. Soc. **90**, 673 (2007).

[16] L. Tang, N. M. Anoop Krishnan, J. Berjikian, J. Rivera, M. M. Smedskjaer, J. C. Mauro, W. Zhou, and M. Bauchy, Effect of nanoscale phase separation on the fracture behavior of glasses: Toward tough, yet transparent glasses, Phys. Rev. Mater. **2**, 113602 (2018).

[17] D. G. Burnett and R. W. Douglas, Liquid-liquid phase separation in the soda-lime-silica system, Phys. Chem. Glasses **11**, 125 (1970).

[18] L. Martel, M. Allix, F. Millot, V. Sarou-Kanian, E. Véron, S. Ory, D. Massiot, and M. Deschamps, Controlling the size of nanodomains in calcium aluminosilicate glasses, J. Phys. Chem. C **115**, 18935 (2011).

[19] W. Haller, D. H. Blackburn, F. E. Wagstaff, and R. J. Charles, Metastable immiscibility surface in the system Na_2O-B_2O_3-SiO_2, J. Am. Ceram. Soc. **53**, 34 (1970).

[20] B. R. Wheaton and A. G. Clare, Evaluation of phase separation in glasses with the use of atomic force microscopy, J. Non-Cryst. Solids **353**, 4767 (2007).

[21] N. Kreidl, Phase separation in glasses, J. Non-Cryst. Solids **129**, 1 (1991).

[22] P. F. James, Liquid-phase separation in glass-forming systems, J. Mater. Sci. **10**, 1802 (1975).

[23] M. E. Nordberg, Properties of some Vycor-brand glasses, J. Am. Ceram. Soc. **27**, 299 (1944).

[24] A. K. Varshneya, *Fundamentals of Inorganic Glasses* (Academic Press, San Diego, 1994).

[25] S. M. Ohlberg, H. R. Golob, J. J. Hammel, and R. R. Lewchuk, Noncrystalline microphase separation in soda-lime-silica glass, J. Am. Ceram. Soc. **48**, 331 (1965).

[26] Y. Xiang and J. Du, Effect of strontium substitution on the structure of 45S5 bioglasses, Chem. Mater. **23**, 2703 (2011).

[27] A. N. Cormack, J. Du, and T. R. Zeitler, Alkali ion migration mechanisms in silicate glasses probed by molecular dynamics simulations, Phys. Chem. Chem. Phys. **4**, 3193 (2002).

[28] T. R. Zeitler and A. N. Cormack, Interaction of water with bioactive glass surfaces, J. Cryst. Growth **294**, 96 (2006).

[29] O. Laurent, B. Mantisi, and M. Micoulaut, Structure and topology of soda-lime silicate glasses: Implications for window glass, J. Phys. Chem. B **118**, 12750 (2014).

[30] J. Du and A. N. Cormack, The medium range structure of sodium silicate glasses: A molecular dynamics simulation, J. Non-Cryst. Solids **349**, 66 (2004).

[31] J. Du and A. N. Cormack, Erratum to 'The medium range structure of sodium silicate glasses: a molecular dynamics simulation' by J. Du and A. N. Cormack [J. Non-Cryst. Solids 349 (2004) 66–79], J. Non-Cryst. Solids **351**, 956(E) (2005).

[32] S. Plimpton, Fast parallel algorithms for short-range molecular dynamics, J. Comput. Phys. **117**, 1 (1995).

[33] W. M. Brown, P. Wang, S. J. Plimpton, and A. N. Tharrington, Implementing molecular dynamics on hybrid high performance computers - short range forces, Comput. Phys. Commun. **182**, 898 (2011).

[34] W. M. Brown, A. Kohlmeyer, S. J. Plimpton, and A. N. Tharrington, Implementing molecular dynamics on hybrid high performance computers - Particle-particle particle-mesh, Comput. Phys. Commun. **183**, 449 (2012).

[35] A. Stukowski, Visualization and analysis of atomistic simulation data with OVITO - the Open Visualization Tool, Model. Simul. Mater. Sci. Eng. **18**, 015012 (2010).

[36] L. Cormier, G. Calas, and B. Beuneu, Structural changes between soda-lime silicate glass and melt, J. Non-Cryst. Solids **357**, 926 (2011).

[37] S. Urata, R. Ando, M. Ono, and Y. Hayashi, Molecular dynamics study on nano-particles reinforced oxide glass, J. Am. Ceram. Soc. **101**, 2266 (2018).

[38] V. F. Sears, Neutron scattering lengths and cross sections, Neutron News **3**, 26 (1992).

[39] A. C. Wright, The comparison of molecular dynamics simulations with diffraction experiments, J. Non-Cryst. Solids **159**, 264 (1993).

[40] X. Li, W. Song, K. Yang, N. M. A. Krishnan, B. Wang, M. M. Smedskjaer, J. C. Mauro, G. Sant, M. Balonis, and M. Bauchy, Cooling rate effects in sodium silicate glasses: Bridging the gap between molecular dynamics simulations and experiments, J. Chem. Phys. **147**, 074501 (2017).

[41] D. I. Grimley, A. C. Wright, and R. N. Sinclair, Neutron scattering from vitreous silica IV. Time-of-flight diffraction, J. Non-Cryst. Solids **119**, 49 (1990).

[42] J. I. Gersten and F. W. Smith, *The Physics and Chemistry of Materials* (Wiley, New York, 2001).

[43] D. J. Green, *An Introduction to the Mechanical Properties of Ceramics* (Cambridge University Press, Cambridge, 1998).

[44] L. Brochard, G. Hantal, H. Laubie, F.-J. Ulm, and R. J.-M. Pellenq, Fracture mechanisms in organic-rich shales: Role of kerogen, in *Poromechanics V: Proceedings of the Fifth Biot Conference on Poromechanics*, edited by C. Hellmich, B. Pichler, and D. Adam (American Society of Civil Engineers, Reston, VA, 2013), p. 2471.

[45] B. Wang, Y. Yu, Y. J. Lee, and M. Bauchy, Intrinsic nanoductility of glasses: The critical role of composition, Front. Mater. **2**, 11 (2015).

[46] M. Wang, B. Wang, T. K. Bechgaard, J. C. Mauro, S. J. Rzoska, M. Bockowski, M. M. Smedskjaer, and M. Bauchy, Crucial effect of angular flexibility on the fracture toughness and nanoductility of aluminosilicate glasses, J. Non-Cryst. Solids **454**, 46 (2016).

[47] T. To, S. S. Sørensen, J. F. S. Christensen, R. Christensen, L. R. Jensen, M. Bockowski, M. Bauchy, and M. M. Smedskjaer, Bond switching in densified oxide glass enables record-high fracture toughness, ACS Appl. Mater. Interfaces **13**, 17753 (2021).

[48] L. Brochard, G. Hantal, H. Laubie, F.-J. Ulm, and R. J.-M. Pellenq, Capturing material toughness by molecular simulation: Accounting for large yielding effects and limits, Int. J. Fract. **194**, 149 (2015).

[49] T. To, S. S. Sørensen, M. Stepniewska, A. Qiao, L. R. Jensen, M. Bauchy, Y. Yue, and M. M. Smedskjaer, Fracture toughness of a metal-organic framework glass, Nat. Commun. **11**, 2593 (2020).

[50] M. Bauchy, H. Laubie, M. J. A. Qomi, C. G. Hoover, F.-J. Ulm, and R. J.-M. Pellenq, Fracture toughness of calcium-silicate-hydrate from molecular dynamics simulations, J. Non-Cryst. Solids **419**, 58 (2015).

[51] A. Stukowski, Computational analysis methods in atomistic modeling of crystals, JOM **66**, 399 (2014).

[52] P. S. Mann, *Introductory Statistics*, 8th ed. (Wiley, New York, 2013).

[53] C. Hermansen, J. Matsuoka, S. Yoshida, H. Yamazaki, Y. Kato, and Y. Z. Yue, Densification and plastic deformation

under microindentation in silicate glasses and the relation to hardness and crack resistance, J. Non-Cryst. Solids **364**, 40 (2013).

[54] T. Deschamps, J. Margueritat, C. Martinet, A. Mermet, and B. Champagnon, Elastic moduli of permanently densified silica glasses, Sci. Rep. **4**, 7193 (2014).

[55] M. N. Svenson, M. Guerette, L. Huang, N. Lönnroth, J. C. Mauro, S. J. Rzoska, M. Bockowski, and M. M. Smedskjaer, Universal behavior of changes in elastic moduli of hot compressed oxide glasses, Chem. Phys. Lett. **651**, 88 (2016).

[56] See Supplemental Material at http://link.aps.org/supplemental/10.1103/PhysRevMaterials.5.093602 for further details about structural and mechanical properties of the simulated glasses as well as additional snapshots of the atomic configuration during the fracture simulations.

[57] M. Yamane and T. Sakaino, Chemical composition of phase-separated droplets in soda-lime-silica glass, J. Am. Ceram. Soc. **51**, 178 (1968).

[58] F. C. Serbena and E. D. Zanotto, Internal residual stresses in glass-ceramics: A review, J. Non-Cryst. Solids **358**, 975 (2012).

[59] M. O. C. Villas-Boas, F. C. Serbena, V. O. Soares, I. Mathias, and E. D. Zanotto, Residual stress effect on the fracture toughness of lithium disilicate glass-ceramics, J. Am. Ceram. Soc. **103**, 465 (2020).

[60] O. Peitl, E. D. Zanotto, F. C. Serbena, and L. L. Hench, Compositional and microstructural design of highly bioactive P_2O_5-Na_2O-CaO-SiO_2 glass-ceramics, Acta Biomater. **8**, 321 (2012).

[61] M. Guerette and L. Huang, A simple and convenient set-up for high-temperature Brillouin light scattering, J. Phys. D: Appl. Phys. **45**, 275302 (2012).

[62] F. Yuan and L. Huang, Brittle to ductile transition in densified silica glass, Sci. Rep. **4**, 5035 (2014).

[63] S. M. Wiederhorn, Fracture surface energy of glass, J. Am. Ceram. Soc. **52**, 99 (1969).

[64] T. To, F. Célarié, C. Roux-Langlois, A. Bazin, Y. Gueguen, H. Orain, M. Le Fur, V. Burgaud, and T. Rouxel, Fracture toughness, fracture energy and slow crack growth of glass as investigated by the Single-Edge Precracked Beam (SEPB) and Chevron-Notched Beam (CNB) methods, Acta Mater. **146**, 1 (2018).